RESEARCH ARTICLE SUMMARY

BIOCHEMISTRY

Structure of the nucleotide exchange factor eIF2B reveals mechanism of memory-enhancing molecule

Jordan C. Tsai,* Lakshmi E. Miller-Vedam,* Aditya A. Anand,* Priyadarshini Jaishankar, Henry C. Nguyen, Adam R. Renslo, Adam Frost,† Peter Walter†

INTRODUCTION: Regulation by the integrated stress response (ISR) converges on the phosphorylation of translation initiation factor eIF2 in response to a variety of stresses. Phosphorylation converts eIF2 from a substrate to a competitive inhibitor of its dedicated guanine nucleotide exchange factor, eIF2B, inhibiting translation. ISRIB is a drug-like eIF2B activator that reverses the effects of eIF2 phosphorylation, enhances cognition, and corrects cognitive deficits after brain injury in rodents. Because ISRIB shows promise for treating neurological disorders a deeper understanding of its mechanism of action is crucial. Previous work identified eIF2B as a target of ISRIB and suggested that the molecule stabilizes and activates the enzyme. However, the molecule's mode of binding and means of activation remain unknown.

RATIONALE: To identify the binding site and mechanism of action of ISRIB, we used cryo–electron microscopy (cryo-EM) to determine an atomic-resolution structure of decameric human eIF2B bound to ISRIB. We validated the structural model using mutational analysis and the synthesis of ISRIB analogs. Combined with pre–steady-state kinetic analysis of eIF2B complex assembly, these findings enabled us to derive a functional model of ISRIB action.

RESULTS: A robust recombinant expression and purification protocol for all subunits of human eIF2B produced a stable eIF2B holoenzyme that sedimented as a decamer. Under conditions of elevated ionic strength, an eIF2Bα dimer [eIF2B(α_2)] dissociated from the remainder of the decamer, whereas ISRIB prevented disassembly. Sedimentation velocity experiments determined that in the absence of eIF2Bα, the remaining subunits form tetrameric complexes [eIF2B($\beta\gamma\delta\varepsilon$)]. Loss of eIF2B($\alpha_2$) largely abolished eIF2B's nucleotide exchange activity. To explain these findings, we determined a structure of human eIF2B bound to ISRIB at 2.8 Å average resolution. The structure revealed that ISRIB binds within a deep cleft at a two-fold symmetry interface between the eIF2Bβ and eIF2Bδ subunits in the decamer.

Greater resolution within the binding pocket enabled precise positioning of ISRIB, which we validated by probing with designed ISRIB analogs and mutational analysis. For example, stereospecific addition of a methyl group to ISRIB abrogated activity, whereas an eIF2B(δL179A) mutation accommodated this analog and restored activity. Further, a predicted C-H-π interaction between eIF2B(βH188) and ISRIB was confirmed by mutation of βH188 to other aromatic residues, which resulted in enhanced stability of the complex. To determine how ISRIB enhances incorporation of eIF2B(α_2) into the complex, we analyzed the eIF2B($\beta\gamma\delta\varepsilon$) tetramer structurally and functionally. Cryo-EM imaging and analytical ultracentrifugation revealed that ISRIB staples two eIF2B($\beta\gamma\delta\varepsilon$) tetramers together to form an octamer across its two-fold symmetry axis. The resulting octamer displays a composite surface for avid eIF2B(α_2) binding, explaining ISRIB's mechanism of action. Consistent with this model, saturating half-binding sites in the tetramer with ISRIB prevented dimerization and failed to activate the enzyme. Additional loss-of-function and gain-of-function dimerization mutants produced complexes that were insensitive to ISRIB.

CONCLUSION: From this work, the regulation of eIF2B assembly from stable subcomplexes emerges as a rheostat for eIF2B activity that tunes translation during the ISR and can be further modulated by ISRIB acting as a "molecular staple." As a two-fold symmetric small molecule, ISRIB bridges a central symmetry axis of the decameric eIF2B complex, stabilizing it in an activated state. ISRIB's action as an assembly-promoting enzyme activator provides a plausible model for its ability to ameliorate the inhibitory effects of eIF2α phosphorylation. Understanding the different modes of regulation of this vital translational control point will be of particular importance in the nervous system where ISRIB has been shown to have a range of effects, and will further enable ISRIB's development as a promising therapeutic agent in combating cognitive disorders. ■

ON OUR WEBSITE

Read the full article at http://dx.doi.org/10.1126/science.aaq0939

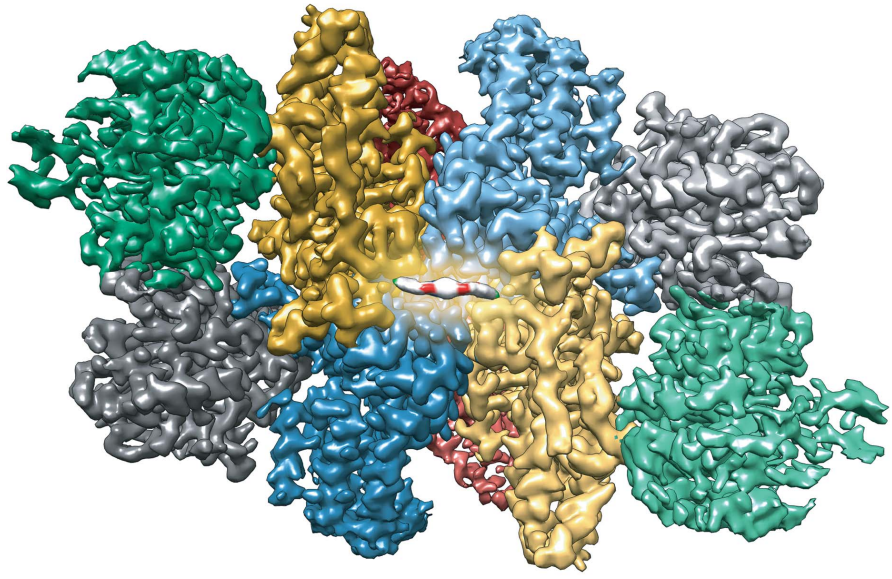

ISRIB bound to human eIF2B. View of cryo-EM density for eIF2B$(\alpha\beta\gamma\delta\varepsilon)_2$, colored in distinct shades for each subunit copy: (red, α; blue, β; green, γ; gold, δ; gray, ε). Density assigned to ISRIB is depicted in CPK coloring (red, O; blue, N; green, Cl) and artistically contrasted from its target protein.

The list of author affiliations is available in the full article online.
*These authors contributed equally to this work.
†Corresponding author. Email: peter@walterlab.ucsf.edu (P.W.); adam.frost@ucsf.edu (A.F.)
Cite this article as J. C. Tsai *et al.*, *Science* **359**, eaaq0939 (2018). DOI: 10.1126/science.aaq0939

RESEARCH ARTICLE

BIOCHEMISTRY

Structure of the nucleotide exchange factor eIF2B reveals mechanism of memory-enhancing molecule

Jordan C. Tsai,[1,2]* Lakshmi E. Miller-Vedam,[2,3]* Aditya A. Anand,[1,2]* Priyadarshini Jaishankar,[4] Henry C. Nguyen,[2,3] Adam R. Renslo,[4] Adam Frost,[2,3]† Peter Walter[1,2]†

Regulation by the integrated stress response (ISR) converges on the phosphorylation of translation initiation factor eIF2 in response to a variety of stresses. Phosphorylation converts eIF2 from a substrate to a competitive inhibitor of its dedicated guanine nucleotide exchange factor, eIF2B, thereby inhibiting translation. ISRIB, a drug-like eIF2B activator, reverses the effects of eIF2 phosphorylation, and in rodents it enhances cognition and corrects cognitive deficits after brain injury. To determine its mechanism of action, we solved an atomic-resolution structure of ISRIB bound in a deep cleft within decameric human eIF2B by cryo–electron microscopy. Formation of fully active, decameric eIF2B holoenzyme depended on the assembly of two identical tetrameric subcomplexes, and ISRIB promoted this step by cross-bridging a central symmetry interface. Thus, regulation of eIF2B assembly emerges as a rheostat for eIF2B activity that tunes translation during the ISR and that can be further modulated by ISRIB.

Protein quality control is essential to the maintenance of cellular and organismal health. To prevent the production of deleterious proteins, such as those from invading viruses or those produced in misfolding-prone environments, cells regulate protein synthesis. By arresting or accelerating the cardinal decision of translation initiation, cells effect proteome-wide changes that drive organismal functions such as development, memory, and immunity (*1*–*3*).

A key enzyme in the regulation of protein synthesis is eukaryotic translation initiation factor 2B (eIF2B), a dedicated guanine nucleotide exchange factor (GEF) for translation initiation factor 2 (eIF2). eIF2B is composed of five subunits (α, β, γ, δ, ε) that assemble into a decamer composed of two copies of each subunit (*4*–*8*). The eIF2Bε subunit contains the enzyme's catalytic center and associates closely with eIF2Bγ (*9*). Two copies each of the structurally homologous eIF2Bα, β, and δ subunits form the regulatory core that modulates eIF2B's catalytic activity (*10*–*12*). eIF2B's substrate, eIF2, is composed of three subunits (α, β, γ) and binds methionine initiator tRNA and guanosine triphosphate (GTP) to form the ternary complex required to initiate translation on AUG start codons. eIF2's γ subunit contains the GTP-binding pocket [reviewed in (*13*, *14*)].

In response to various inputs, many of which are cell stresses, phosphorylation of eIF2α at Ser^{51} converts eIF2 from a substrate for nucleotide exchange into a competitive inhibitor of eIF2B. Phosphorylated eIF2 binds to eIF2B with enhanced affinity, effectively sequestering the limiting eIF2B complex from engaging unphosphorylated eIF2 for nucleotide exchange (*10*–*12*). Such inhibition leads to an attenuation of general translation and, paradoxically, the selective translation of stress-responsive mRNAs that contain small upstream open reading frames. This latter set includes mRNAs that encode transcriptional activators such as ATF4 (*15*, *16*). In this way, eIF2 phosphorylation elicits an intricate gene expression program. This pathway was termed the "integrated stress response" after the discovery of several kinases that all phosphorylate eIF2α at Ser^{51} to integrate different physiological signals, such as the accumulation of misfolded proteins in the lumen of the endoplasmic reticulum, the accumulation of double-stranded RNA indicative of viral infection, the cell's redox status, and nutrient availability (*17*).

We previously identified an ISR inhibitor (ISRIB) that reverses the effects of eIF2α phosphorylation, restoring translation in stressed cells and blocking translation of ISR-activated mRNAs such as ATF4 (*18*, *19*). When administered systemically to wild-type rodents, ISRIB enhances cognition, leading to significant improvements in spatial and fear-associated learning (*18*). This effect relies on translation-dependent remodeling of neuronal synapses (*20*). eIF2 phosphorylation correlates with diverse neurodegenerative diseases and cancers as well as normal aging (*21*–*24*). In addition, a number of mutations that impair eIF2B activity lead to a neurodegenerative disorder of childhood known as vanishing white matter disease (VWMD), which is marked by cerebellar ataxia, spasticity, hypersensitivity to head trauma and infection, coma, and premature death (*25*). As a well-characterized small molecule with rapid cross–blood-brain barrier equilibration, reasonable bioavailability, and good tolerability in rodent efficacy models, ISRIB and related analogs offer great potential for treating VWMD and a range of other devastating diseases lacking therapeutic options (*18*, *26*). Indeed, in rodents, ISRIB entirely reverses cognitive deficits associated with traumatic brain injuries (*27*) and protects against neurodegeneration (*26*).

Previous work identified eIF2B as the molecular target of ISRIB (*28*, *29*). ISRIB enhances eIF2B GEF activity by a factor of 3, stabilizes a decameric form of the enzyme when analyzed in high-salt conditions, and increases thermostability of the eIF2Bδ subunit (*28*). Mutations that render cells insensitive to ISRIB have been found to cluster in the N-terminal region of eIF2Bδ (*29*); when projected onto the crystal structure of *Schizosaccharomyces pombe* eIF2B, two of the mutated residues map to its symmetric interface (*8*). These data hinted that ISRIB may activate eIF2B by binding near adjacent δ subunits to exert its blunting effects on the ISR. Here, we report mechanistic and structural insights into ISRIB's mechanism of action.

ISRIB stabilizes decameric eIF2B, thereby accelerating GEF activity

To investigate the mechanism by which ISRIB enhances the GEF activity of eIF2B, we engineered a recombinant *Escherichia coli* expression system for coexpression of all five subunits of human eIF2B (Fig. 1A). eIF2B purified as a monodisperse complex that sedimented at 13.6*S*, corresponding to the size of a decamer containing two copies of each subunit (Fig. 1B and fig. S1A).

We adapted a fluorescent guanosine diphosphate (GDP) exchange assay (*29*) to assess the enzymatic activity of recombinant eIF2B. We purified the substrate, nonphosphorylated human eIF2, from a *Saccharomyces cerevisiae* expression system genetically edited to lack the only yeast eIF2 kinase (*gcn2*Δ) (*30*) (fig. S2, A and B). First, in a "GDP loading assay," we added fluorescent Bodipy-GDP to GDP-bound eIF2. We observed an eIF2B concentration–dependent increase in fluorescence corresponding to the dislodging of bound GDP and subsequent binding of Bodipy-GDP to eIF2 (fig. S2, C and D). Second, in a "GDP unloading assay," we chased with a 1000-fold excess of unlabeled GDP and measured a decrease in fluorescence corresponding to the eIF2B-catalyzed dissociation of Bodipy-GDP from eIF2 (fig. S2E). GEF activities were fit to a single-exponential curve (fig. S2F) for calculating the observed rate constants (k_{obs}). Titrating substrate concentration to saturating levels in GDP unloading assays yielded Michaelis constant (K_m)

[1]Howard Hughes Medical Institute, University of California, San Francisco, CA, USA. [2]Department of Biochemistry and Biophysics, University of California, San Francisco, CA, USA. [3]Chan Zuckerberg Biohub, San Francisco, CA, USA. [4]Department of Pharmaceutical Chemistry and Small Molecule Discovery Center, University of California, San Francisco, CA, USA.
*These authors contributed equally to this work.
†Corresponding author. Email: peter@walterlab.ucsf.edu (P.W.); adam.frost@ucsf.edu (A.F.)

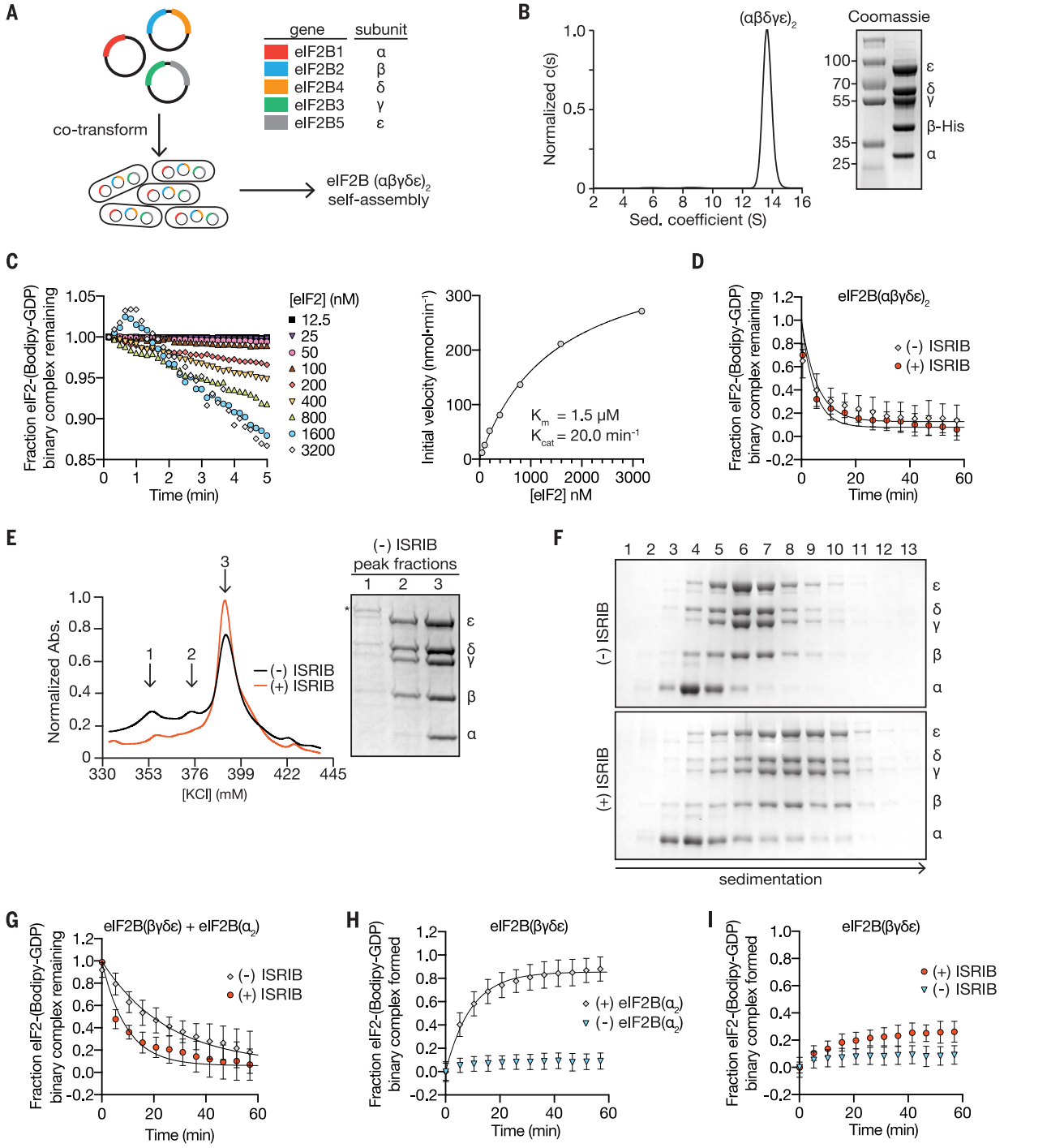

Fig. 1. ISRIB stabilizes decameric eIF2B, accelerating GEF activity. (**A**) Schematic diagram for three-plasmid expression of all five eIF2B genes in *E. coli*. (**B**) Characterization of eIF2B$(\alpha\beta\gamma\delta\epsilon)_2$ by sedimentation velocity analytical ultracentrifugation and SDS–polyacrylamide gel electrophoresis (PAGE) followed by Coomassie Blue staining. (**C**) Initial rate of nucleotide exchange (right) plotted as a function of substrate concentration. Note that at high eIF2 concentrations, we reproducibly observed a transient increase in fluorescence that peaked at the 1-min time point (left). Such an increase was reported previously (*29*) and remains unexplained. (**D**) GEF activity of eIF2B$(\alpha\beta\gamma\delta\epsilon)_2$ as measured by unloading of fluorescent GDP from eIF2 in the presence and absence of ISRIB (mean ± SD; $n = 3$). (**E**) Representative absorbance 280-nm traces from an anion exchange column used in the purification of eIF2B in the presence (red) and absence (black) of ISRIB ($n = 3$). Traces were normalized to total protein eluted in respective runs. Peak fractions from the −ISRIB purification were analyzed by SDS-PAGE and Coomassie-stained. eIF2B subunits are labeled α to ε; an asterisk denotes the presence of a contaminating protein that contributes to peak 1. (**F**) Stability of eIF2B$(\alpha\beta\gamma\delta\epsilon)_2$ was assessed by sedimentation velocity on a 5 to 20% sucrose gradient in 400 mM salt buffer. eIF2B$(\beta\gamma\delta\epsilon)$ and eIF2B(α_2) were combined with and without 500 nM ISRIB. Fractions were analyzed by SDS-PAGE and Coomassie staining. (**G**) GEF activity of eIF2B assembled from purified eIF2B$(\beta\gamma\delta\epsilon)$ and eIF2B (α_2) in the presence and absence of ISRIB (mean ± SD; $n = 3$). (**H**) GEF activity of eIF2B$(\beta\gamma\delta\epsilon)$ in the presence and absence of eIF2B(α_2) (mean ± SD; $n = 3$). (**I**) GEF activity of eIF2B$(\beta\gamma\delta\epsilon)$ in the presence and absence of ISRIB (mean ± SD; $n = 3$).

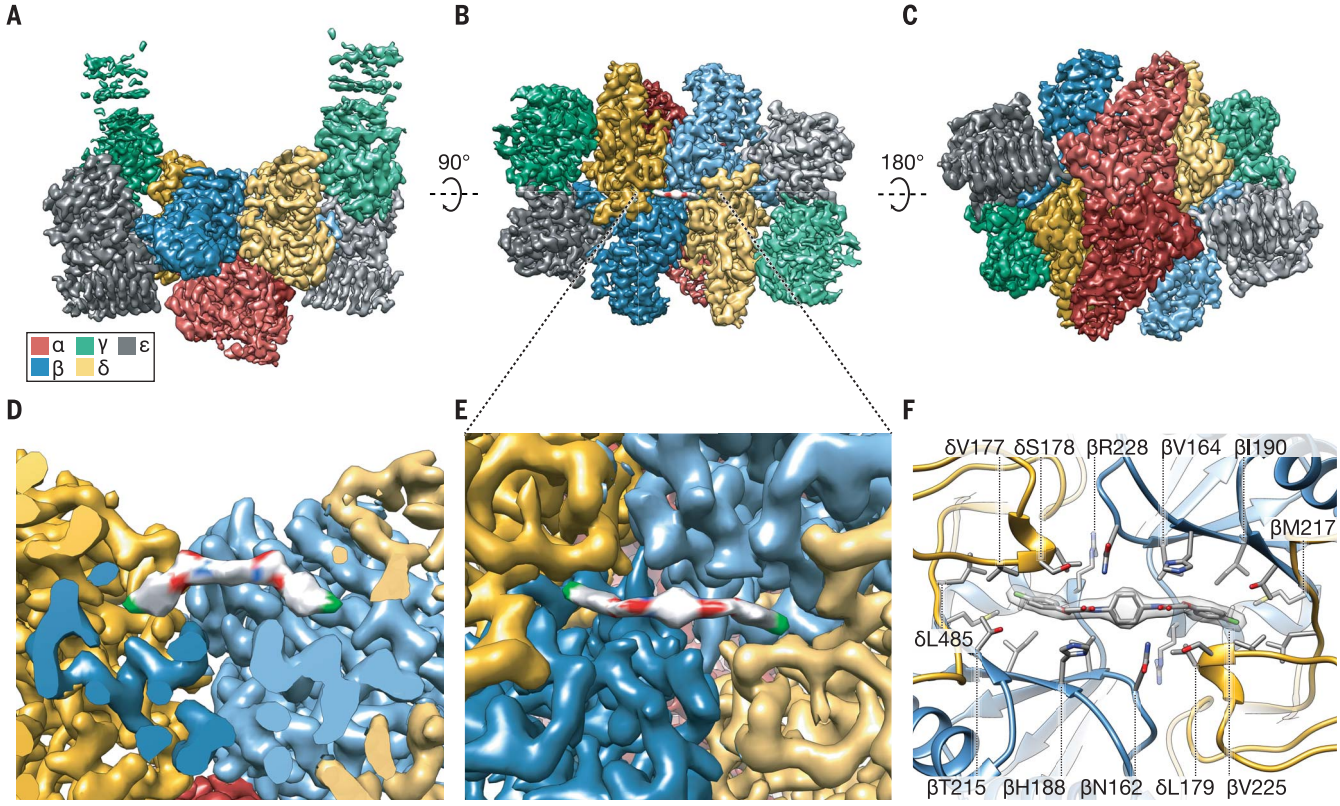

Fig. 2. Atomic-resolution reconstruction of ISRIB-bound eIF2B. (**A** to **C**) Three views of cryo-EM density for eIF2B$(\alpha\beta\gamma\delta\varepsilon)_2$, colored in distinct shades for each subunit copy (red, α; blue, β; green, γ; gold, δ; gray, ε). Density assigned to ISRIB is depicted in CPK coloring (red, O; blue, N; green, Cl). The rotational relationships between the views depicted in (A), (B), and (C) are indicated. (**D**) Cross section of (A), revealing the ISRIB binding pocket at the central decamer symmetry interface and density assigned to ISRIB CPK-colored by element. (**E**) Close-up view of density assigned to ISRIB and its binding pocket in (B) at the intersection of two β and two δ subunits. (**F**) Two conformers of ISRIB modeled into the density. All residues within 3.7 Å of the ligand are rendered as sticks.

and catalytic rate constant (k_{cat}) values similar to those of eIF2B previously purified from mammalian cells (Fig. 1C) (*31*).

To investigate how ISRIB activates eIF2B, we fixed eIF2B and eIF2 in a multi-turnover regime at concentrations of 10 nM and 1 μM, respectively. Under these conditions, eIF2 is subsaturating given its K_m of 1.5 μM (Fig. 1C). Previously, a factor of 3 stimulation of nucleotide exchange by ISRIB was seen under similar conditions (*28*). Surprisingly, ISRIB only marginally activated the recombinant eIF2B decamer by a factor of 1.2 (Fig. 1D; –ISRIB, k_{obs} = 0.17 ± 0.006 min^{-1}; +ISRIB, k_{obs} = 0.21 ± 0.005 min^{-1}).

ISRIB stabilizes eIF2B decamers in lysates of human embryonic kidney (HEK) 293T cells (*28*), suggesting a role during assembly of the active complex. To test this notion and its implications for ISRIB's mechanism of action, we purified eIF2B in the presence or absence of ISRIB. Under both conditions, we obtained the fully assembled decamer (Fig. 1E, peak 3); however, in the absence of ISRIB, we also obtained a partially assembled complex lacking the α subunit that eluted from the anion exchange column at a lower ionic strength (Fig. 1E, peak 2). These data suggest that ISRIB enhances the stability of the decamer. To test this idea, we expressed eIF2B(βγδε) and eIF2Bα separately (fig. S1, B and C). Surprisingly, eIF2B(βγδε) purified as a heterotetramer, as determined by analytical ultracentrifugation (fig. S1D), whereas eIF2Bα purified as a homodimer, as previously observed (fig. S1E) (*6*). We then combined eIF2B(βγδε) and eIF2B(α_2) under stringent conditions of elevated ionic strength (400 mM) to assess ISRIB's contribution to the stability of the decameric complex. When analyzed by velocity sedimentation in the absence of ISRIB, eIF2B(βγδε) sedimented as a tetramer (peak fractions 6 and 7), whereas eIF2B(α_2) peaked in fraction 4 (Fig. 1F, top). By contrast, in the presence of ISRIB, eIF2B(βγδε) and eIF2B(α_2) sedimented together as a higher–molecular weight complex deeper in the gradient (peak fractions 7 to 9) (Fig. 1F, bottom). As we discuss below, the stabilized decamer peaked in fraction 10 of the gradient, indicating that under these conditions, the decamer partially dissociates during sedimentation. We surmise that dissociation during centrifugation led to the broad sedimentation profiles observed. Thus, ISRIB enhanced the stability of decameric eIF2B.

To study the interplay among ISRIB binding, eIF2B(α_2) incorporation into the decamer, and GEF activity, we mixed independently purified eIF2B(α_2) and eIF2B(βγδε) subcomplexes and assayed the combination for GDP unloading. When assayed under these conditions, the specific activity was reduced by a factor of 4 relative to the fully assembled decamer (compare Fig. 1D and Fig. 1G, k_{obs} = 0.17 ± 0.006 min^{-1} versus 0.04 ± 0.009 min^{-1}). The addition of ISRIB restored GEF activity toward the level of fully assembled decamer by a factor of 3 (k_{obs} = 0.11 ± 0.002 min^{-1}) (Fig. 1G), which suggests that ISRIB's activity reflects enhanced decamer stability.

Using the GDP loading assay, we found that eIF2B activity was reduced profoundly (k_{obs} = 0.01 ± 0.007 min^{-1}) in the absence of eIF2B(α_2) (Fig. 1H), as previously reported (*32*, *33*). Interestingly, ISRIB still activated eIF2B(βγδε) (Fig. 1I, k_{obs} = 0.04 ± 0.003 min^{-1}), indicating that ISRIB can enhance GEF activity independent of eIF2B(α_2) incorporation into the holoenzyme. To reconcile these unexpected findings, we next sought a structural understanding of the ISRIB-stabilized human eIF2B decameric complex.

ISRIB binds in a deep cleft, bridging the two-fold symmetric interface of the eIF2B decamer

We determined an atomic-resolution structure of eIF2B bound to ISRIB by cryo–electron microscopy (cryo-EM). We classified and refined a single consensus structure from 202,125 particles to an

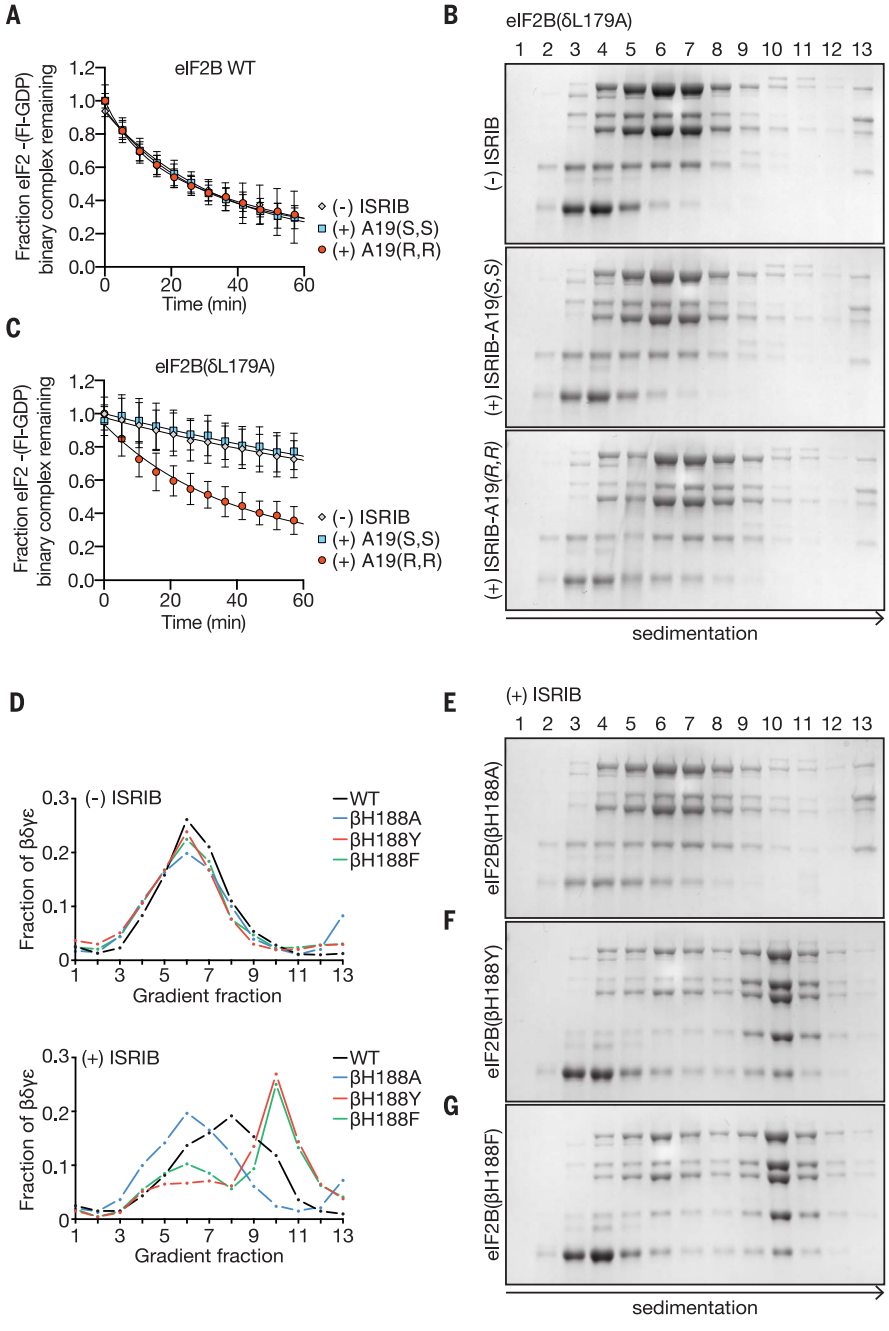

Fig. 3. eIF2B structure predicts activity of ISRIB analogs. (**A**) GEF activity of assembled eIF2B(βγδε) and eIF2B(α_2) in the presence and absence of ISRIB-A19(*R*,*R*) and ISRIB-A19(*S*,*S*) (mean ± SD; *n* = 3). (**B**) Stability of decameric eIF2B(δL179A) in the absence of ISRIB (top), presence of ISRIB-A19(*S*,*S*) (middle), or presence of ISRIB-A19(*R*,*R*) (bottom) as assessed by velocity sedimentation on sucrose gradients. (**C**) eIF2B GEF activity of assembled eIF2B(βγδε) and eIF2B(α_2) containing a δL179A mutation in the presence and absence of ISRIB-A19(*R*,*R*) and ISRIB-A19(*S*,*S*) (mean ± SD; *n* = 3). (**D**) Quantification of eIF2B decamer stability gradients plotted as fraction of eIF2B(βγδε) present in each of lanes 1 to 13 in (E) to (G). eIF2B (for comparison from data shown in Fig. 1F), eIF2B(βH188A), eIF2B(βH188Y), and eIF2B (βH188F) gradients are plotted in the presence (bottom) and absence (top) of 500 nM ISRIB. (**E** to **G**) Stability of decameric eIF2B(βH188A), eIF2B(βH188Y), and eIF2B(βH188F) in the presence of ISRIB, as assessed by velocity sedimentation on sucrose gradients.

average resolution of 2.8 Å, which varied from 2.7 Å in the stable core to >3.4 Å in the more flexible periphery (fig. S3). The overall structure bears clear resemblance to the *S. pombe* two-fold symmetric decameric structure determined by x-ray crystallography (*8*). The symmetry interface comprises contacts between the α, β, and δ subunits, while the γ and ε subunits are attached at opposing ends (Fig. 2, A to C). As in the *S. pombe* crystal structure, the catalytic HEAT domains of the ε subunits were not resolved, indicating their flexible attachment to the regulatory core. By contrast, densities for the "ear" domains of the γ subunits were resolved, but at a resolution that precluded atomic interpretation (Fig. 2B and figs. S3 and S4).

We observed a clearly defined density consistent with the dimensions of ISRIB and not attributable to protein bridging the symmetry interface of the decamer (Fig. 2, B, D, and E, and fig. S5). Modeling suggests that ISRIB binds with its central cyclohexane ring in the expected low-energy chair conformation, with the side chains projecting to the same face of the cyclohexane ring and inserting the distal 4-chlorophenyl rings into deep binding pockets (Fig. 2, D to F, and fig. S5). ISRIB's "U-shaped" conformation may be stabilized by intramolecular N-H···O hydrogen-bonding interactions between its amide nitrogen N-H bond and the aryl ether oxygens, possibly explaining why non–ether-linked congeners of ISRIB are much less potent (fig. S6) (*28*, *34*). The cryo-EM density most likely corresponds to an average of at least two energetically equivalent ISRIB conformations related by 180° rotations about both N-C bonds to the cyclohexane ring (both depicted in Fig. 2F and figs. S4 and S5). This superposition of two conformers accounts for the apparently symmetric density observed, even though in isolation each individual conformer is pseudo-symmetric (fig. S5). The multiple observed ISRIB binding modes may contribute to its free energy of binding by providing additional entropic wiggle room.

The N-terminal loop of the δ subunit contributes key residues to the binding pocket, and this loop differs from the ligand-free *S. pombe* structure (*8*). Residues in the δ loop are important for ISRIB activity (*29*), including Val^{177} and Leu^{179} (δV177 and δL179), which contribute directly to the hydrophobic surface of the binding pocket (Fig. 2F and fig. S6). In addition, the δ subunits contribute δL485 to the hydrophobic wells that accommodate the halogenated benzene rings (Fig. 2F and fig. S6). The center of the binding site comprises residues from the β subunit, including Asn^{162} and His^{188} (βN162 and βH188), which lie near ISRIB's more polar functionality. In particular, one of the two C-H bonds at the glycolamide α-carbon is oriented perpendicular to the plane of the aromatic histidine ring (Fig. 2F and fig. S6), suggesting a C-H-π interaction with βH188. Residues on the β subunits, including Val^{164} and Ile^{190} (βV164 and βI190), also make key contributions to the hydrophobicity of the deep wells.

Thus, ISRIB enhances incorporation of the α subunit into the decamer despite not making direct contacts with this subunit. Rather, ISRIB stabilizes the symmetry interface of the β-δ core, which in turn favors stable eIF2B(α_2) binding. As such, ISRIB's enhancement of GEF activity derives from its ability to promote higher-order holoenzyme assembly.

Structural model predicts the activity of modified compounds and mutations

To validate the structural model, we synthesized ISRIB analogs bearing a methyl group at the α

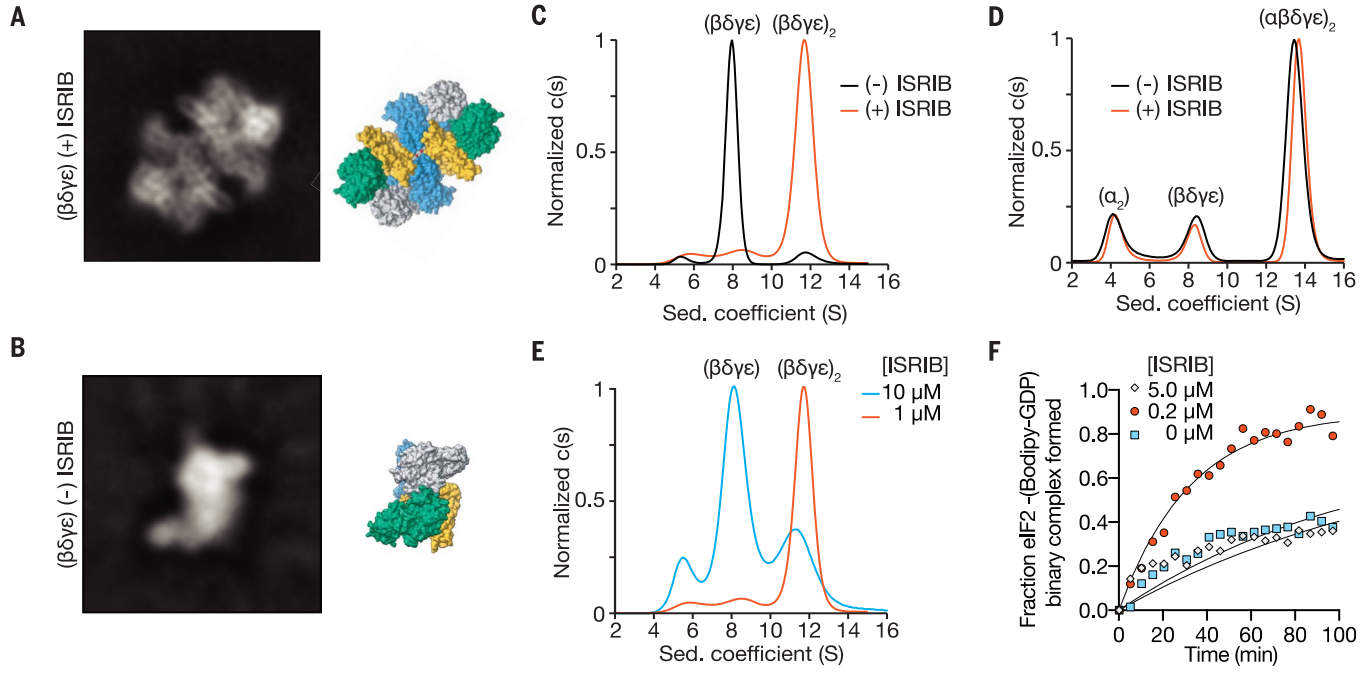

Fig. 4. ISRIB induces dimerization of tetrameric eIF2B subcomplexes. (**A** and **B**) The most abundant 2D class averages from cryo-EM imaging of eIF2B(βγδε) in the presence (A) and absence (B) of ISRIB. Subunit colors are as in Fig. 2. (**C**) Characterization of eIF2B(βγδε) by sedimentation velocity analytical ultracentrifugation. eIF2B(βγδε) (1 μM) was analyzed in the presence and absence of 1 μM ISRIB. (**D**) Mixture of 1 μM eIF2B(βγδε) and 500 nM eIF2B(α_2) characterized by analytical ultracentrifugation in the presence and absence of 1 μM ISRIB. (**E**) eIF2B(βγδε) (1 μM) characterized by analytical ultracentrifugation in the presence of 1 μM or 10 μM ISRIB. (**F**) GEF activity of eIF2B(βγδε), here at a higher concentration (100 nM) to facilitate comparison of 0, 0.2, and 5 μM ISRIB.

position of the glycolamide side chains. Two enantiomers, ISRIB-A19(*R*,*R*) and ISRIB-A19(*S*,*S*), were prepared (fig. S7A) on the basis of predicted steric clashes with residue δL179 for ISRIB-A19(*R*,*R*) or βH188 for ISRIB-A19(*S*,*S*) in the ISRIB binding pocket (Fig. 2F and fig. S6). As expected, neither enantiomer enhanced GEF activity in vitro or in cells (Fig. 3A and fig. S7B), nor did they enhance the stability of purified decameric eIF2B (fig. S7C). We next engineered eIF2B to accommodate the additional methyl groups on ISRIB-A19(*R*,*R*) by mutating δL179 to alanine (δL179A). We tested the effects of both compounds on eIF2B(δL179A) by velocity sedimentation and GEF activity. As predicted, ISRIB-A19(*R*,*R*) stabilized formation of mutant decamers (Fig. 3B) and stimulated nucleotide exchange (Fig. 3C). Treatment with ISRIB-A19(*R*,*R*) activated eIF2B(δL179A) by approximately a factor of 3 (Fig. 3C, k_{obs} = 0.027 ± 0.001 min^{-1}), similar to the activation of wild-type eIF2B by ISRIB. By contrast, and as predicted, ISRIB-A19(*S*,*S*) failed to activate eIF2B(δL179A) (Fig. 3C, k_{obs} = 0.007 ± 0.001 min^{-1}). Notably, in the absence of ISRIB analogs, eIF2B(δL179A) was less active than eIF2B by a factor of 5 (compare Fig. 3A and Fig. 3C; eIF2B k_{obs} = 0.04 ± 0.009 min^{-1}, eIF2B(δL179A) k_{obs} = 0.008 ± 0.002 min^{-1}). This result identifies δL179A as a novel hypomorphic mutation and underscores the importance of this surface for holoenzyme assembly.

We next sought to verify the existence of a putative C-H-π interaction between βH188 and ISRIB by mutating βH188 to alanine. As predicted, ISRIB did not stabilize eIF2B(βH188A) decamers (Fig. 3, D and E, and fig. S8). By contrast, although mutation of βH188 to an aromatic tyrosine (βH188Y) or phenylalanine (βH188F) was predicted to sustain and likely enhance C-H-π interactions, it did not impair ISRIB's activity to stabilize decamers (Fig. 3, D, F, and G, and fig. S8). Rather, ISRIB stabilized eIF2B(βH188Y) and eIF2B(βH188F) decamers to an even greater extent than wild-type eIF2B decamers (Fig. 3D). Whereas ISRIB-stabilized wild-type eIF2B sedimented with a broad profile, indicating dissociation of the decamer through the course of sedimentation (Figs. 1F and 3D), ISRIB-stabilized eIF2B(βH188Y) and eIF2B(βH188F) formed a sharp symmetric peak in fraction 10, indicative of enhanced complex integrity through sedimentation, presumably owing to enhanced C-H-π bonding interaction with ISRIB (Fig. 3, D, F, and G, and fig. S8).

ISRIB induces dimerization of tetrameric eIF2B subcomplexes

Because ISRIB bridges the symmetry interface of the decamer without making direct contacts with eIF2B(α_2), we sought to understand how the small molecule promotes eIF2B(α_2) incorporation into the decamer. We imaged purified eIF2B(βγδε) tetramers in the presence and absence of ISRIB by cryo-EM. In the presence of ISRIB, the images revealed a predominant species consistent with an octameric complex of eIF2B lacking the α subunits (Fig. 4A). By contrast, in the absence of ISRIB, the predominant species was consistent with a tetrameric complex divided along the symmetry axis of the octamer (Fig. 4B). In accordance with the ISRIB-dependent stabilization of the decamer by mutations in βH188 to other aromatic residues, βH188F and βH188Y mutants also stabilized the octamer in high-salt conditions (fig. S9). These images suggest a model in which ISRIB dimerizes eIF2B(βγδε) by "stapling" the tetramers together to form the octameric binding platform for α subunit binding, consistent with the architecture of the ISRIB-bound decamer.

We next substantiated eIF2B(βγδε) dimerization by analytical ultracentrifugation under physiological salt conditions. In the absence of ISRIB, eIF2B(βγδε) sedimented as a predominant 8.0*S* peak and a minor 11.7*S* peak, corresponding to eIF2B(βγδε) and eIF2B$(βγδε)_2$, respectively (Fig. 4C). By contrast, in the presence of ISRIB, we observed a marked increase in the 11.7*S* peak, demonstrating ISRIB's role in stabilizing the eIF2B$(βγδε)_2$ octamer. Together with the observation that eIF2B(βγδε) has greater activity in the presence of ISRIB (Fig. 1I), these data show the importance of octamer assembly in activating GEF activity.

Dimerization of eIF2B(βγδε) effectively doubles the surface area for eIF2B(α_2) binding, which suggests that the ISRIB-enhanced incorporation of eIF2B(α_2) into the decamer originates from ISRIB's ability to shift the tetramer/octamer equilibrium. To test this prediction, we combined eIF2B(α_2) and eIF2B(βγδε) in the presence and absence of ISRIB and assessed decamer assembly

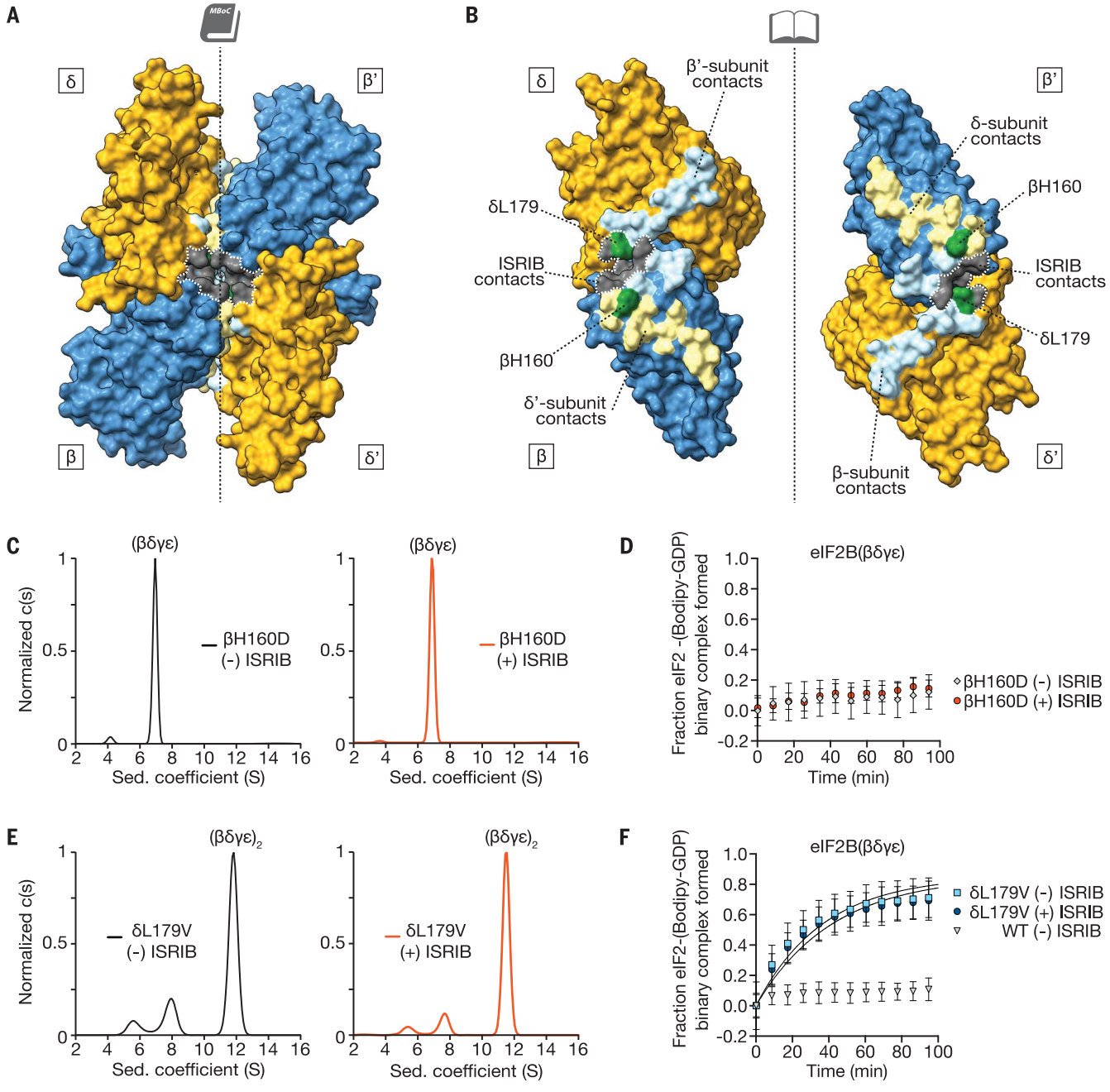

Fig. 5. Loss- and gain-of-function dimerization mutants resist or bypass the effects of ISRIB. (**A**) Surface rendering of core eIF2Bβ (blue) and eIF2Bδ (gold) subunits; residues contacting ISRIB are highlighted in gray, and the dimer interface is indicated by a dashed line. Interface residues are highlighted in a lighter hue of the colors of the contacting subunits. (**B**) Open-book view of the dimer-dimer interface, such that each β and δ subunit is rotated by 90°. βH160, in green, contacts both β′ and δ′; δL179, also in green, contacts both β′ and ISRIB. (**C**) Characterization of 1 μM eIF2B(βγδε) containing a βH160D mutation in the presence (right) and absence (left) of 1 μM ISRIB by analytical ultracentrifugation. (**D**) GEF activity of eIF2B(βγδε) containing a βH160D mutation in the presence and absence of ISRIB (mean ± SD; n = 3). (**E**) Characterization of 1 μM eIF2B(βγδε) containing a δL179V mutation in the presence (right) and absence (left) of 1 μM ISRIB by analytical ultracentrifugation. (**F**) GEF activity of eIF2B(βγδε) containing a δL179V mutation in the presence and absence of ISRIB (mean ± SD; n = 3).

by analytical ultracentrifugation. Under the high protein concentrations used in these assays, we observed a predominant peak corresponding to the assembled eIF2B decamer at 13.6*S* both in the presence and absence of ISRIB, together with minor peaks corresponding to unincorporated eIF2B(βγδε) at 8.0*S* and eIF2B(α_2) at 4.1*S* (Fig. 4D). We did not observe an octamer peak, which suggests that the octamer has a high affinity for eIF2B(α_2) and assembles the full decamer under these conditions. Together with the cryo-EM images, these data demonstrate that eIF2B(α_2) and ISRIB synergistically promote dimerization of eIF2B(βγδε).

Given that ISRIB binds across the eIF2B$(\beta\gamma\delta\varepsilon)_2$ interface such that each tetramer contributes half of the ISRIB binding site, we reasoned that high ISRIB concentrations may occupy half-sites within the tetramers and interfere with octamer formation. Indeed, ISRIB promoted eIF2B$(\beta\gamma\delta\varepsilon)_2$ assembly at 1 μM but failed to do so at 10 μM

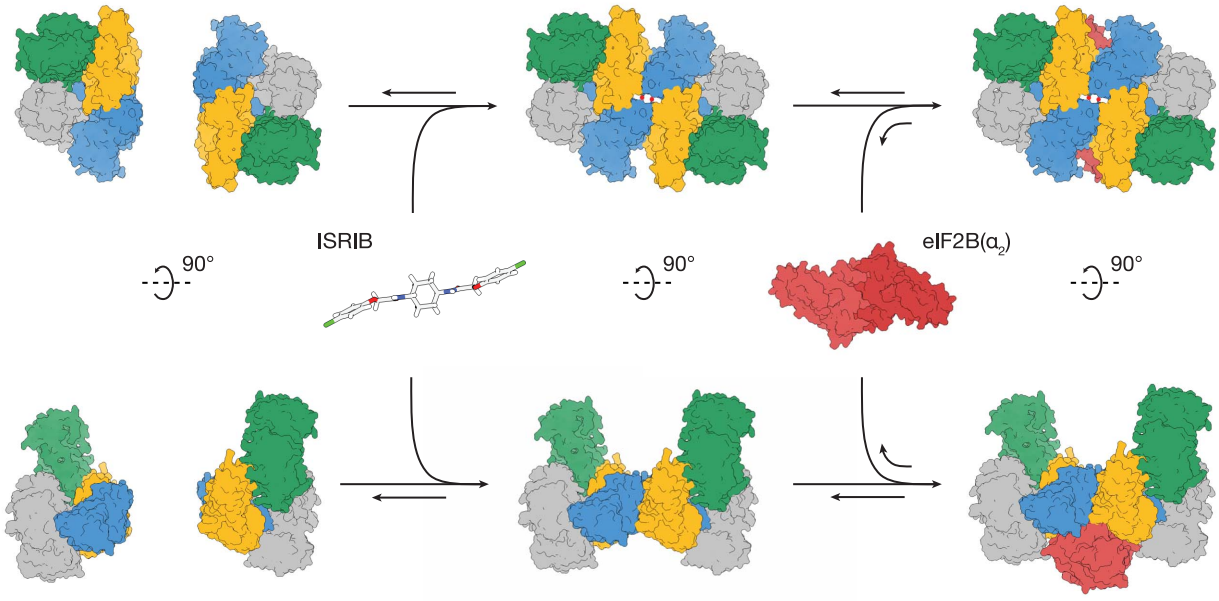

Fig. 6. Model for ISRIB's mechanism of action. ISRIB staples together tetrameric eIF2B(βγδε) subcomplexes, building a more active eIF2B(βγδε)$_2$ octamer. In turn, the ISRIB-stabilized octamer binds eIF2B(α_2) with greater affinity, enhancing the formation of a fully active, decameric holoenzyme.

(Fig. 4E). Similarly, ISRIB stimulated GEF activity of eIF2B(βγδε) at 0.2 μM but failed to do so at 5 μM (Fig. 4F). Note that the high ISRIB concentrations used in this assay did not reduce GEF activity below that of eIF2B(βγδε); this shows that the effect did not result from nonspecific enzymatic inhibition.

Loss- and gain-of-function dimerization mutants resist or bypass the effects of ISRIB

To visualize the determinants of octamerization, we highlighted the solvent-excluded surface area along the symmetry interface of the β and δ subunits in adjacent tetramers (Fig. 5, A and B, light yellow, light blue, green) and labeled the residues of the ISRIB binding pocket on this surface (Fig. 5, A and B, gray). The tetramer-tetramer contact residues form a thin strip along each neighboring β and δ subunit. Most of the β subunit residues contact the δ subunit across the symmetry interface, while a small number of residues also cement β-β′ contacts. Of these, His^{160} (βH160) and Arg^{228} (βR228) reside at the junction of β-β′ and β-δ′ subunits, which suggests that they play key roles in stabilizing the octamer. Accordingly, we observed that mutation of βH160 to aspartic acid, which we predicted would be repulsed by δD450, completely precluded octamer assembly. Analytical ultracentrifugation of eIF2B(βγδε) containing the βH160D mutation revealed a sharp tetramer peak at 7*S* both in the absence and presence of ISRIB (Fig. 5C), and ISRIB was unable to enhance GEF activity for this mutant (Fig. 5D). Thus, the effect of this mutation on octamerization cannot be overcome by ISRIB binding, even though ISRIB binding buries an additional ~11% of solvent-exposed surface area—an increase from 3420 Å^2 to 3790 Å^2—upon stapling of tetramers (Fig. 5, A and B).

Serendipitously, we also identified a gain-of-function mutation in eIF2B. We initially engineered a δL179V mutation alongside the δL179A mutation used above to accommodate the methylated analog ISRIB-A19(*R*,*R*) (Fig. 2F and fig. S6). To our surprise, we discovered that the predominant species of δL179V-eIF2B(βγδε) sedimented as a remarkably stable octamer in the absence of ISRIB (Fig. 5E). GEF activity assays revealed that δL179V-eIF2B(βγδε)$_2$ was 5 times as active as the wild-type octamers formed in the presence of ISRIB, and was not further activated by ISRIB (compare Fig. 5F and Fig. 1I; eIF2B(δL179V) k_{obs} = 0.027 ± 0.001 min^{-1}, eIF2B(δL179V) + ISRIB k_{obs} = 0.024 ± 0.001 min^{-1}, wild-type + ISRIB k_{obs} = 0.005 ± 0.001 min^{-1}). Together with the ISRIB-bound structure, these mutants indicate that the major contribution of ISRIB to increased GEF activity lies at the step of tetramer dimerization and assembly of the bipartite surface for α subunit homodimer binding (Fig. 6).

Discussion

We determined the structure of human eIF2B at sufficiently high resolution to characterize the binding site and coordination of a small molecule with therapeutic potential. In concomitant work, Zyryanova *et al.* report similar findings (*35*). The atomic model of ISRIB-bound eIF2B reconciles structure-activity relationships described previously (*28*, *34*), predicted both loss- and gain-of-function mutations, and facilitates the rational design of small-molecule modulators of eIF2B activity. The structure provides an intuitive view of how ISRIB activates nucleotide exchange: ISRIB stabilizes the active decameric form of the eIF2B holoenzyme by stapling the constituents together across a two-fold symmetry axis.

Given that a catalytic residue essential for nucleotide exchange resides in the still-unresolved HEAT repeat of the ε subunit, how does assembly of the decameric holoenzyme enhance activity? Cross-linking studies suggest that eIF2 binds across the decameric interface, engaging the eIF2B α subunit along with β and δ subunits from opposing tetramers (*8*). We surmise that decamer assembly creates a composite surface for eIF2 binding that allows the flexibly attached HEAT domain to reach and engage its target. Although we consider it likely that the effects of ISRIB binding can be explained by the degree of holoenzyme assembly, additional ligand-induced allosteric changes may also contribute to its activity.

These observations provide a plausible model for ISRIB's ability to ameliorate the inhibitory effects of eIF2α phosphorylation on ternary complex formation. ISRIB staples tetrameric building blocks together into an octamer, which enhances activity by a factor of 3 and forms a platform for association of the dimeric α subunits. The integrated effect of these sequential steps is an enhancement of activity by an order of magnitude. The inhibition resulting from a limiting amount of phosphorylated eIF2 would be reduced by the surplus of GEF activity provided by ISRIB. By contrast, an excess of ISRIB poisons the assembly reaction by saturating half-binding sites on unassembled tetramers. Thus, within its effective concentration range, ISRIB will enhance ternary complex formation even in unstressed conditions, opening an untapped reservoir of additional enzymatic capacity. We surmise that in vivo these activities are likely to be realized near the equilibrium points of the assembly reactions for the holoenzyme, allowing for ISRIB's observed phenotypic effects. Thus, eIF2B is poised to integrate diverse signals that affect translation initiation.

Phosphorylation of eIF2 may be just one of many mechanisms for modulating its activity. Posttranslational modifications, expression of other modulatory components, or binding of unidentified endogenous ligands (to the ISRIB binding pocket or elsewhere) are likely to modulate eIF2B activity under varying physiological conditions. Understanding the different modes of regulation of this vital translational control point will be of particular importance in the nervous system, where ISRIB has been shown to have a range of effects.

Materials and methods

Cloning of eIF2B expression plasmids

The five human eIF2B subunits were *E. coli* codon–optimized and synthesized on the BioXp 3200 System (SGI-DNA) in six blunt-end dsDNA fragments; see supplementary materials for synthesized sequences. Fragments were cloned into pCR-BluntII-TOPO vector with the Zero Blunt TOPO PCR Cloning Kit (Invitrogen) and verified by sequencing. In brief, subunits of eIF2B were PCR-amplified from TOPO cloned vectors and Infusion (Clontech) cloned into multigene expression plasmids with compatible drug resistances and origins of replication: pETDuet-1 (Novagen 71146-3), pACYCDuet-1 (Novagen 71147-3), or pCOLADuet-1 (Novagen 71406-3) vectors. Each expression plasmid contains two cloning sites (site 1 and site 2), enabling simultaneous expression of up to two genes per plasmid. eIF2B1 (encoding the α subunit) was inserted into site 1 of pETDuet-1 (pJT066). eIF2B2 (encoding the β subunit) and eIF2B4 (encoding the δ subunit) were inserted into sites 1 and 2 of pACYCDuet-1, respectively (pJT073). eIF2B3 (encoding the γ subunit) and eIF2B5 (encoding the ε subunit) were inserted into sites 1 and 2 of pCOLADuet-1, respectively (pJT074). eIF2B5 was synthesized in two fragments eIF2B5_1 and eIF2B5_2 that were simultaneously inserted into site 2 by Infusion.

Purification of decameric eIF2B(αβδγε)$_2$

pJT066, pJT073, and pJT074 were cotransformed into One Shot BL21 Star (DE3) chemically competent *E. coli* cells (Invitrogen) and grown in Luria broth containing ampicillin, kanamycin, and chloramphenicol at 37°C on an orbital shaker. When the culture reached an OD_{600} of 0.6, the temperature was reduced to 16°C, and the culture was induced with 0.8 mM IPTG (Gold Biotechnology) and grown for 16 hours. Cells were harvested and lysed with EmulsiFlex-C3 (Avestin) in a buffer containing 20 mM HEPES-KOH, pH 7.5, 250 mM KCl, 1 mM tris(2-carboxyethyl)phosphine (TCEP), 5 mM $MgCl_2$, 15 mM imidazole, and complete EDTA-free protease inhibitor cocktail (Roche). The lysate was clarified at 30,000*g* for 20 min at 4°C. Subsequent purification steps were conducted on the ÄKTA Pure (GE Healthcare) system at 4°C.

The clarified lysate was loaded onto a HisTrap HP 5 ml, washed in binding buffer (20 mM HEPES-KOH, pH 7.5, 200 mM KCl, 1 mM TCEP, 5 mM $MgCl_2$, and 15 mM imidazole), and eluted with a linear gradient (75 ml) of 15 mM to 300 mM imidazole in the same buffer. The eIF2B fraction eluted from the HisTrap column at 80 mM imidazole. The eIF2B fraction was collected and loaded onto a 20 ml Mono Q HR16/10 column (GE Healthcare), washed in Buffer A (20 mM HEPES-KOH, pH 7.5, 200 mM KCl, 1 mM TCEP, and 5 mM $MgCl_2$) and eluted with a linear gradient (200 ml) of 200 mM to 500 mM KCl in the same buffer. The eIF2B fraction eluted off the Mono Q column at a conductivity of 46 mS/cm (corresponding to 390 mM KCl). Fractions were collected, concentrated with an Amicon Ultra-15 concentrator (EMD Millipore) with a 100,000-dalton molecular weight cutoff, and loaded onto a Superdex 200 10/300 GL column (GE Healthcare) equilibrated with Buffer A. A typical preparation yielded approximately 0.5 mg of eIF2B(αβδγε)$_2$ from a 1-liter culture.

EM sample preparation and data collection

Decameric eIF2B(αβγδε)$_2$ + ISRIB: After size exclusion chromatography, eIF2B(αβγδε)$_2$ was diluted to 500 nM and a stock solution of 200 μM ISRIB in *N*-methyl-2-pyrrolidone (NMP) was added to a final ISRIB concentration of 2 μM in a final solution containing 20 mM HEPES-KOH, pH 7.5, 200 mM KCl, 1 mM TCEP, 5 mM $MgCl_2$, 0.5% NMP, and incubated on ice for 10 min. This sample was applied to either C-Flat 1.2/1.3-2C grids (EMS, USA) or Quantifoil R 1.2/1.3 200 Au mesh grids (Quantifoil, Germany). C-flat grids were used without additional cleaning or glow discharging. Quantifoil grids were soaked in chloroform for 30 min and desiccated overnight in a fume hood before use without glow discharging. Using a Vitrobot Mark IV at 4°C and 100% humidity, 3.5 μl of sample was applied to the grid, incubated for an additional 10 s, then blotted with –0.5 mm offset for ~6 s and plunge-frozen in liquid ethane. Two data sets were collected on different microscopes. The first data set was collected with the 300-kV Titan Krios 2 at the HHMI Janelia Research Campus using a K2 Summit detector operated in super-resolution mode; 1780 images were collected at a magnification of 29,000× (0.51 Å per pixel) as dose-fractionated stacks of 67 × 0.15-s exposures (1.19 $e^-/Å^2$) for a total dose of ~80 $e^-/Å^2$ (table S1). The second data set was collected with the 300-kV Titan Krios at UC Berkeley using a K2 Summit detector operated in super-resolution mode; 1515 images were collected at a magnification of 29,000× (0.42 Å per pixel) as dose-fractionated stacks of 27 × 0.18-s exposures (1.83 $e^-/Å^2$) for a total dose of ~44 $e^-/Å^2$ (table S1).

Tetrameric eIF2B(αβγδ) ± ISRIB: After size exclusion chromatography, tetrameric eIF2B(αβγδ) was diluted to 800 nM and vitrified in the absence of ISRIB and in the presence of 2 μM ISRIB, as described above, but with ~4 s blot time; 129 micrographs of ligand-free and 67 micrographs of ISRIB-bound sample were collected on the 200 kV Talos Arctica at UCSF at 36,000× using a K2 Summit detector operated in super-resolution mode (1.15 Å/pixel).

Image analysis and 3D reconstruction

All dose-fractionated image stacks were corrected for motion artefacts, 2× binned in the Fourier domain, and dose-weighted using MotionCor2 (*36*), resulting in one dose-weighted and one unweighted integrated image per stack with pixel sizes of 1.02 Å (Janelia) or 0.838 Å (UC Berkeley). The parameters of the contrast transfer function (CTF) were estimated using GCTF-v1.06 (*37*) and the motion-corrected but unweighted images; ~1000 particles per data set were manually selected and averaged in 2D using RELION 2.0 (*38*). The resulting class sums were then used as templates for automated particle picking using Gautomatch-v0.55 (*37*), followed by extraction and rescaling to a common pixel size of 0.838 Å and four rounds of 2D classification (table S2).

For the 3D reconstruction of decameric eIF2B(αβγδε)$_2$ + ISRIB, the resulting subset of particles were input into cryoSPARC (*39*) to compute an ab initio reconstruction without symmetry, followed by homogeneous refinement in both cryoSPARC (dynamic masking) and in RELION 2.0 (unmasked) with no symmetry. Subsequent heterogeneous refinement (cryoSPARC) or multiclass 3D classification (RELION 2.0) removed less than 1% of the remaining particles (table S1).

High-resolution homogeneous refinement was then performed in parallel in cryoSPARC, RELION 2.1, and FREALIGN (*40*) using soft-edged masks and imposed C2 symmetry (figs. S3 and S4). All three approaches yielded maps of similar visual quality that differed in numerical resolution by ~0.1 Å, as measured by Fourier shell correlation. All three maps were low-pass filtered and sharpened using automated procedures and used comparatively during model building in COOT and PHENIX (see below). Molecular graphics and analyses were performed with the UCSF Chimera package and the FREALIGN map. Chimera is developed by the Resource for Biocomputing, Visualization, and Informatics at UCSF [supported by NIGMS P41-GM103311 (*41*)]. The map-versus-model FSC plots were generated using the FREALIGN map (see below and fig. S4). Accession numbers for the human eIF2B structures determined with FREALIGN, cryoSPARC, and RELION, respectively, are as follows: EMD-7442, EMD-7443, EMD-7444 (density maps; Electron Microscopy Data Bank) and 6CAJ (coordinates of atomic models; Protein Data Bank).

Atomic modeling and validation

An initial model of the human complex was generated using one-to-one threading as implemented in Phyre2 (*42*) using from the *S. pombe* crystal structure [PDB: 5B04 (*8*)] structure for the β, γ, δ, and ε subunits and the *H. sapiens* crystal structure [PDB: 3ECS (*43*)] for the α subunit. The initial ISRIB ligand model was generated in PHENIX eLBOW (*44*) using the SMILES, manually adjusted in COOT (*45*), and then refined with phenix.real_space_refine (*46*) using global minimization and simulated annealing. This initial model was manually adjusted in COOT a second time and further refined in phenix.real_space_refine using global minimization, secondary structure restraints, and local grid search. This model was manually adjusted a third and final time in COOT,

minimized in phenix.real_space_refine with per-residue B-factors, and the final model statistics were tabulated using Molprobity (*47*) (table S3). Map versus atomic model FSC plots for the entire decamer and the isolated βδβ′δ′ chains were computed using EMAN 2 (*48*) using calculated density maps from e2pdb2mrc.py with heteroatoms (ISRIB) and per-residue B-factor weighting. Solvent accessible surfaces and buried surface areas were calculated from the atomic models using UCSF ChimeraX. Final atomic models have been deposited at the PDB with accession code 6CAJ.

Cloning of mutant eIF2B expression plasmids

Mutant eIF2B constructs were generated by site-directed mutagenesis on pJT073 using the primer indicated and its reverse complement.

δL179A (pJT091): 5′-tacggttctaaagtttctgctttctct-cacctgccgcag-3′

βH188A (pJT089): 5′-gctgctcgtaaacgtaaattcgctgt-tatcgttgctgaatgcgct-3′

βH188F (pJT094): 5′-gctcgtaaacgtaaattcttcgttat-cgttgctgaatg-3′

βH188Y (pJT095): 5′-gctgctcgtaaacgtaaattctacgt-tatcgttgctgaatg-3′

δL179V (pJT090): 5′-tacggttctaaagtttctgttttctctc-acctgccgcag-3′

βH160D (pJT102): 5′-caggctctggaacacatcgactct-aacgaagttatcatg-3′

Purification of tetrameric eIF2B(βδγε)

Tetrameric eIF2B(βδγε) and tetrameric eIF2B(βδγε) mutant proteins were purified using the same protocol as described for the decamer with the exception that expression strains were cotransformed without the eIF2B α subunit expressing plasmid. A typical preparation yielded approximately 0.75 mg of eIF2B(βδγε) from a 1 liter culture.

eIF2B(βδγε) tetramer with co-transformed plasmids: pJT073, pJT074

δL179A eIF2B(βδγε) tetramer with co-transformed plasmids: pJT091, pJT074

βH188A eIF2B(βδγε) tetramer with co-transformed plasmids: pJT089, pJT074

βH188F eIF2B(βδγε) tetramer with co-transformed plasmids: pJT094, pJT074

βH188Y eIF2B(βδγε) tetramer with co-transformed plasmids: pJT095, pJT074

δL179V eIF2B(βδγε) tetramer with co-transformed plasmids: pJT090, pJT074

βH160D eIF2B(βδγε) tetramer with co-transformed plasmids: pJT102, pJT074

Purification of eIF2B(α_2)

Purification of the eIF2B(α_2) was adapted from previously published purifications (*6*, *43*). The α subunit was N-terminally tagged with a 6×His tag followed by a TEV cleavage site (pJT075). pJT075 was transformed into BL21 (DE3) *E. coli* cells and grown in Luria broth containing ampicillin at 37°C on an orbital shaker. When the culture reached an OD_{600} of 0.8, the temperature was reduced to 20°C, induced with 0.8 mM IPTG, and grown for 16 hours. Cells were harvested and lysed in a buffer containing 20 mM HEPES-KOH, pH 7.5, 250 mM KCl, 1 mM TCEP, 5 mM $MgCl_2$, 20 mM imidazole, and 1× protease inhibitor cocktail, and clarified at 30,000*g* for 20 min at 4°C.

The clarified lysate was loaded onto a 5-ml HisTrap HP column, washed in a buffer containing 20 mM HEPES-KOH, pH 7.5, 30 mM KCl, 1 mM TCEP, 5 mM $MgCl_2$, and 20 mM imidazole, and eluted with 75-ml linear gradient of 20 to 300 mM imidazole. The HisTrap elution was then passed through a MonoQ HR 16/10 and subsequently a MonoS HR 10/10 (GE Healthcare), both equilibrated in a buffer containing 20 mM HEPES-KOH, pH 7.5, 30 mM KCl, 1 mM TCEP, and 5 mM $MgCl_2$. eIF2B(α_2) was collected in the flow-through fractions of both MonoQ and MonoS columns. The eIF2B(α_2) containing fraction was incubated for 16 hours at 4°C with TEV protease (50 μg of TEV per liter of culture) and passed through on a 5-ml HisTrap HP. Cleaved eIF2B(α_2) was recovered in the flow-through fraction, concentrated with an Amicon Ultra-15 concentrator (EMD Millipore) with a 30,000-dalton molecular mass cutoff and chromatographed on a Superdex 75 10/300 GL (GE Healthcare) column equilibrated in a buffer containing 20 mM HEPES-KOH, pH 7.5, 200 mM KCl, 1 mM TCEP, 5 mM $MgCl_2$, and 5% glycerol. A typical preparation yielded approximately 0.3 mg of eIF2B(α_2) from a 1-liter culture.

Preparation of human eIF2

Human eIF2 was prepared from an established recombinant *S. cerevisiae* expression protocol (*30*). In brief, the yeast strain GP6452 (gift from the Pavitt lab, University of Manchester) containing yeast expression plasmids for human eIF2 subunits and a deletion of *GNC2* encoding the only eIF2 kinase in yeast, was grown to saturation in synthetic complete media (Sunrise Science Products) with auxotrophic markers (-Trp, -Leu, -Ura) in 2% dextrose. The β and α subunits of eIF2 were tagged with His6 and FLAG epitopes, respectively. A 12-liter yeast culture was grown in rich expression media containing yeast extract, peptone, 2% galactose, and 0.2% dextrose. Cells were harvested and resuspended in lysis buffer [100 mM Tris, pH 8.5, 300 mM KCl, 5 mM $MgCl_2$, 0.1% NP-40, 5 mM imidazole, 10% glycerol (Thermo Fisher Scientific), 2 mM DTT, 1× protease inhibitor cocktail (Sigma Aldrich #11836170001), 1 μg/ml each aprotinin (Sigma Aldrich), leupeptin (Sigma Aldrich), pepstatin A (Sigma Aldrich). Cells were lysed in liquid nitrogen using a steel blender. The lysate was centrifuged at 10,000*g* for 1 hour at 4°C. Subsequent purification steps were conducted on the ÄKTA Pure (GE Healthcare) system at 4°C. Lysate was applied to a 5-ml HisTrap Crude column (Thermo Fisher Scientific) equilibrated in buffer (100 mM HEPES, pH 7.5, 100 mM KCl, 5 mM $MgCl_2$, 0.1% NP-40, 5% glycerol, 1 mM dithiothreitol, 0.5× protease inhibitor cocktail, 1 μg/ml each aprotinin, leupeptin, pepstatin A). eIF2 bound to the column, was washed with equilibration buffer and eluted using a 50 ml linear gradient of 5 mM to 500 mM imidazole. Eluted eIF2 was incubated with FLAG M2 magnetic affinity beads, washed with FLAG wash buffer (100 mM HEPES, pH 7.5, 100 mM KCl, 5 mM $MgCl_2$, 0.1% NP-40, 5% glycerol, 1 mM TCEP, 1× protease inhibitor cocktail, 1 μg/ml each aprotinin, leupeptin, pepstatin A) and eluted with FLAG elution buffer [identical to FLAG wash buffer but also containing 3× FLAG peptide (100 μg/ml, Sigma Aldrich)]. Concentration of purified protein was measured by BCA assay (Thermo Fisher Scientific # PI23225); protein was flash-frozen in liquid nitrogen and stored in elution buffer at −80° C. A typical preparation yielded 1 mg of eIF2 from a 12-liter culture.

GDP exchange assay

In vitro detection of GDP binding to eIF2 was adapted from a published protocol for a fluorescence intensity–based assay describing dissociation of eIF2 and nucleotide (*29*). We modified the procedure to establish both loading and unloading assays for fluorescent GDP.

For the "GDP loading assay," purified eIF2 (200 pmol) was incubated with a molar equivalent Bodipy-FL-GDP (Thermo Fisher Scientific) in assay buffer (20 mM HEPES, pH 7.5, 100 mM KCl, 5 mM $MgCl_2$, 1 mM TCEP, and 1 mg/ml bovine serum albumin) to a volume of 18 μl in 384 square-well black-walled, clear-bottom polystyrene assay plates (Corning). The reaction was initiated by addition of 2 μl of buffer or purified eIF2B under various conditions to compare nucleotide exchange rates. For comparison of "purified decamer" rates, eIF2B$(\alpha\beta\gamma\delta\varepsilon)_2$ (2 pmol) was preincubated in 0.1% NMP or 0.1% NMP and 2 μM ISRIB for 15 min. These concentrations of vehicle and ISRIB were used throughout, unless otherwise specified. To ensure equal concentrations of GEF catalytic sites in all experiments, comparisons with tetramer used eIF2B(βγδε) (4 pmol). "Assembled decamer" was formed by incubating eIF2B(βγδε) (4 pmol) and eIF2B(α_2) (2 pmol) for 15 min in the presence or absence of ISRIB prior to mixing with substrate eIF2. For the "GDP unloading assay," each reaction was initiated by addition of excess unlabeled GDP (200 nmol). Fluorescence intensity for both loading and unloading assays was recorded every 10 s for 60 or 100 min using a TECAN Infinite M200 Pro plate reader (excitation wavelength: 495 nm, bandwidth 5 nm, emission wavelength: 512 nm, bandwidth: 5 nm). Data collected were fit to a first-order exponential.

Analytical ultracentrifugation

Analytical ultracentrifugation sedimentation velocity experiments were conducted using the ProteomeLab XL-I system (Beckman Coulter) with a Ti60 rotor. Protein samples were loaded into cells in a buffer containing 20 mM HEPES-KOH, pH 7.5, 150 mM KCl, 1 mM TCEP, and 5 mM $MgCl_2$. All runs were conducted at 20°C with a rotor speed of 40,000 rpm. Sedimentation was monitored at an absorbance of 280 nm. Subsequent data analysis was conducted with Sedfit (*49*) using a non–model-based continuous c(s) distribution corrected for time-invariant (TI) and radial-invariant (RI) noise.

Sucrose gradients

Protocol was adapted from a previous study (*28*). Sucrose gradients (5 to 20%, w/v) were prepared by tilted-tube rotation on the Gradient Master 107ip (Biocomp) in a high-salt buffer (20 mM HEPES-KOH, pH 7.5, 400 mM KCl, 1 mM TCEP, and 5 mM $MgCl_2$). Protein samples contained 1 μM eIF2B(βδγε), 500 nM eIF2B(α_2), and 500 nM ISRIB/analog (added from a 500 μM stock solution in NMP to yield a final NMP concentration of 0.1%). For each gradient, 200 μl of sample was loaded and centrifuges in a SW55 rotor (Beckman) for 14 hours at 40,000 rpm, 4°C. Thirteen fractions of 400 μl were collected by aspirating from the top of the gradient, and protein was precipitated by addition of trichloroacetic acid to 15%. After incubation for 90 min on ice, the protein precipitate was collected by centrifugation, and the pellet was resuspended in SDS loading buffer, loaded on a 10% SDS-polyacrylamide gel (Bio-Rad), and after electrophoresis stained with Coomassie Blue. Stained gels were then imaged on a ChemiDoc XRS+ imaging system (Bio-Rad). Quantification of gels was conducted in ImageJ. Fraction of total eIF2B(βγδε) in each of 13 lanes were quantified using a built-in gel-analyzer function. Area under each densitometry plot was calculated and divided by the sum of all areas measured from lanes 1 to 13 to obtain "fraction of eIF2B(βγδε)."

In-cell luciferase assays

Luciferase assays were conducted using a HEK293T cell line carrying an ATF4 luciferase reporter (*18*, *28*). Cells were plated at a density of 30,000 cells per well in a 96-well polylysine-coated plate (Greiner Bio-One). Cells were treated the next day with tunicamycin (1 μg/ml) and varying ISRIB concentrations for 7 hours. Luciferase activity was then assayed using One Glo (Promega) and luminescence quantified in a SpectraMax M5 (Molecular Devices).

REFERENCES AND NOTES

1. R. P. Dalton, D. B. Lyons, S. Lomvardas, Co-opting the unfolded protein response to elicit olfactory receptor feedback. *Cell* **155**, 321–332 (2013). doi: 10.1016/j.cell.2013.09.033; pmid: 24120133
2. M. Costa-Mattioli *et al*., Translational control of hippocampal synaptic plasticity and memory by the eIF2α kinase GCN2. *Nature* **436**, 1166–1173 (2005). doi: 10.1038/nature03897; pmid: 16121183
3. D. H. Munn *et al*., GCN2 kinase in T cells mediates proliferative arrest and anergy induction in response to indoleamine 2,3-dioxygenase. *Immunity* **22**, 633–642 (2005). doi: 10.1016/j.immuni.2005.03.013; pmid: 15894280
4. N. C. Wortham, M. Martinez, Y. Gordiyenko, C. V. Robinson, C. G. Proud, Analysis of the subunit organization of the eIF2B complex reveals new insights into its structure and regulation. *FASEB J.* **28**, 2225–2237 (2014). doi: 10.1096/fj.13-243329; pmid: 24532666
5. Y. Gordiyenko *et al*., eIF2B is a decameric guanine nucleotide exchange factor with a γ2ε2 tetrameric core. *Nat. Commun.* **5**, 3902 (2014). doi: 10.1038/ncomms4902; pmid: 24852487
6. A. M. Bogorad *et al*., Insights into the architecture of the eIF2Bα/β/δ regulatory subcomplex. *Biochemistry* **53**, 3432–3445 (2014). pmid: 24811713
7. B. Kuhle, N. K. Eulig, R. Ficner, Architecture of the eIF2B regulatory subcomplex and its implications for the regulation of guanine nucleotide exchange on eIF2. *Nucleic Acids Res.* **43**, 9994–10014 (2015). pmid: 26384431
8. K. Kashiwagi *et al*., Crystal structure of eukaryotic translation initiation factor 2B. *Nature* **531**, 122–125 (2016). doi: 10.1038/nature16991; pmid: 26901872
9. E. Gomez, S. S. Mohammad, G. D. Pavitt, Characterization of the minimal catalytic domain within eIF2B: The guanine-nucleotide exchange factor for translation initiation. *EMBO J.* **21**, 5292–5301 (2002). doi: 10.1093/emboj/cdf515; pmid: 12356745
10. W. Yang, A. G. Hinnebusch, Identification of a regulatory subcomplex in the guanine nucleotide exchange factor eIF2B that mediates inhibition by phosphorylated eIF2. *Mol. Cell. Biol.* **16**, 6603–6616 (1996). doi: 10.1128/MCB.16.11.6603; pmid: 8887689
11. G. D. Pavitt, K. V. Ramaiah, S. R. Kimball, A. G. Hinnebusch, eIF2 independently binds two distinct eIF2B subcomplexes that catalyze and regulate guanine-nucleotide exchange. *Genes Dev.* **12**, 514–526 (1998). doi: 10.1101/gad.12.4.514; pmid: 9472020
12. T. Krishnamoorthy, G. D. Pavitt, F. Zhang, T. E. Dever, A. G. Hinnebusch, Tight binding of the phosphorylated α subunit of initiation factor 2 (eIF2α) to the regulatory subunits of guanine nucleotide exchange factor eIF2B is required for inhibition of translation initiation. *Mol. Cell. Biol.* **21**, 5018–5030 (2001). doi: 10.1128/MCB.21.15.5018-5030.2001; pmid: 11438658
13. A. G. Hinnebusch, J. R. Lorsch, The mechanism of eukaryotic translation initiation: New insights and challenges. *Cold Spring Harb. Perspect. Biol.* **4**, a011544 (2012). doi: 10.1101/cshperspect.a011544; pmid: 22815232
14. A. G. Hinnebusch, The scanning mechanism of eukaryotic translation initiation. *Annu. Rev. Biochem.* **83**, 779–812 (2014). doi: 10.1146/annurev-biochem-060713-035802; pmid: 24499181
15. H. P. Harding *et al*., Regulated translation initiation controls stress-induced gene expression in mammalian cells. *Mol. Cell* **6**, 1099–1108 (2000). doi: 10.1016/S1097-2765(00)00108-8; pmid: 11106749
16. K. M. Vattem, R. C. Wek, Reinitiation involving upstream ORFs regulates ATF4 mRNA translation in mammalian cells. *Proc. Natl. Acad. Sci. U.S.A.* **101**, 11269–11274 (2004). doi: 10.1073/pnas.0400541101; pmid: 15277680
17. H. P. Harding *et al*., An integrated stress response regulates amino acid metabolism and resistance to oxidative stress. *Mol. Cell* **11**, 619–633 (2003). doi: 10.1016/S1097-2765(03)00105-9; pmid: 12667446
18. C. Sidrauski *et al*., Pharmacological brake-release of mRNA translation enhances cognitive memory. *eLife* **2**, e00498 (2013). doi: 10.7554/eLife.00498; pmid: 23741617
19. C. Sidrauski, A. M. McGeachy, N. T. Ingolia, P. Walter, The small molecule ISRIB reverses the effects of eIF2α phosphorylation on translation and stress granule assembly. *eLife* **4**, (2015). doi: 10.7554/eLife.05033
20. G. V. Di Prisco *et al*., Translational control of mGluR-dependent long-term depression and object-place learning by eIF2α. *Nat. Neurosci.* **17**, 1073–1082 (2014). doi: 10.1038/nn.3754; pmid: 24974795
21. H. P. Harding, D. Ron, in *Translational Control in Biology and Medicine*, M. B. Mathews, N. Sonenberg, J. W. B. Hershey, Eds. (Cold Spring Harbor Laboratory Press, 2007), pp. 345–368.
22. P. Remondelli, M. Renna, The endoplasmic reticulum unfolded protein response in neurodegenerative disorders and its potential therapeutic significance. *Front. Mol. Neurosci.* **10**, 187 (2017). doi: 10.3389/fnmol.2017.00187; pmid: 28670265
23. J. Obacz *et al*., Endoplasmic reticulum proteostasis in glioblastoma—From molecular mechanisms to therapeutic perspectives. *Sci. Signal.* **10**, eaal2323 (2017). doi: 10.7554/eLife.05033
24. G. Martínez, C. Duran-Aniotz, F. Cabral-Miranda, J. P. Vivar, C. Hetz, Endoplasmic reticulum proteostasis impairment in aging. *Aging Cell* **16**, 615–623 (2017). doi: 10.1111/acel.12599; pmid: 28436203
25. P. A. J. Leegwater *et al*., Subunits of the translation initiation factor eIF2B are mutant in leukoencephalopathy with vanishing white matter. *Nat. Genet.* **29**, 383–388 (2001). doi: 10.1038/ng764; pmid: 11704758
26. M. Halliday *et al*., Partial restoration of protein synthesis rates by the small molecule ISRIB prevents neurodegeneration without pancreatic toxicity. *Cell Death Dis.* **6**, e1672–e1679 (2015). doi: 10.1038/cddis.2015.49; pmid: 25741597
27. A. Chou *et al*., Inhibition of the integrated stress response reverses cognitive deficits after traumatic brain injury. *Proc. Natl. Acad. Sci. U.S.A.* **114**, E6420–E6426 (2017). doi: 10.1073/pnas.1707661114; pmid: 28696288
28. C. Sidrauski *et al*., Pharmacological dimerization and activation of the exchange factor eIF2B antagonizes the integrated stress response. *eLife* **4**, e07314 (2015). doi: 10.7554/eLife.07314; pmid: 25875391
29. Y. Sekine *et al*., Mutations in a translation initiation factor identify the target of a memory-enhancing compound. *Science* **348**, 1027–1030 (2015). doi: 10.1126/science.aaa6986; pmid: 25858979
30. R. A. de Almeida *et al*., A yeast purification system for human translation initiation factors eIF2 and eIF2Bε and their use in the diagnosis of CACH/VWM disease. *PLOS ONE* **8**, e53958 (2013). doi: 10.1371/journal.pone.0053958; pmid: 23335982
31. A. G. Rowlands, R. Panniers, E. C. Henshaw, The catalytic mechanism of guanine nucleotide exchange factor action and competitive inhibition by phosphorylated eukaryotic initiation factor 2. *J. Biol. Chem.* **263**, 5526–5533 (1988). pmid: 3356695
32. D. D. Williams, N. T. Price, A. J. Loughlin, C. G. Proud, Characterization of the mammalian initiation factor eIF2B complex as a GDP dissociation stimulator protein. *J. Biol. Chem.* **276**, 24697–24703 (2001). doi: 10.1074/jbc.M011788200; pmid: 11323413
33. B. L. Craddock, C. G. Proud, The α-subunit of the mammalian guanine nucleotide-exchange factor eIF-2B is essential for catalytic activity in vitro. *Biochem. Biophys. Res. Commun.* **220**, 843–847 (1996). doi: 10.1006/bbrc.1996.0495; pmid: 8607853
34. B. R. Hearn *et al*., Structure-activity studies of Bis-O-arylglycolamides: Inhibitors of the integrated stress response. *ChemMedChem* **11**, 870–880 (2016). doi: 10.1002/cmdc.201500483; pmid: 26789650
35. A. F. Zyryanova *et al*., Binding of the integrated stress response inhibitor ISRIB reveals a regulatory site in the nucleotide exchange factor, eIF2B. *Science* **359**, 1533–1536 (2018).
36. S. Q. Zheng *et al*., MotionCor2: Anisotropic correction of beam-induced motion for improved cryo-electron microscopy. *Nat. Methods* **14**, 331–332 (2017). doi: 10.1038/nmeth.4193; pmid: 28250466
37. K. Zhang, Gctf: Real-time CTF determination and correction. *J. Struct. Biol.* **193**, 1–12 (2016). doi: 10.1016/j.jsb.2015.11.003; pmid: 26592709
38. D. Kimanius, B. O. Forsberg, S. H. Scheres, E. Lindahl, Accelerated cryo-EM structure determination with parallelisation using GPUs in RELION-2. *eLife* **5**, e18722 (2016). doi: 10.7554/eLife.18722; pmid: 27845625
39. A. Punjani, J. L. Rubinstein, D. J. Fleet, M. A. Brubaker, cryoSPARC: Algorithms for rapid unsupervised cryo-EM structure determination. *Nat. Methods* **14**, 290–296 (2017). doi: 10.1038/nmeth.4169; pmid: 28165473
40. N. Grigorieff, Frealign: An exploratory tool for single-particle cryo-EM. *Methods Enzymol.* **579**, 191–226 (2016). doi: 10.1016/bs.mie.2016.04.013; pmid: 27572728
41. E. F. Pettersen *et al*., UCSF Chimera—a visualization system for exploratory research and analysis. *J. Comput. Chem.* **25**, 1605–1612 (2004). doi: 10.1002/jcc.20084; pmid: 15264254
42. L. A. Kelley, S. Mezulis, C. M. Yates, M. N. Wass, M. J. E. Sternberg, The Phyre2 web portal for protein modeling, prediction and analysis. *Nat. Protoc.* **10**, 845–858 (2015). doi: 10.1038/nprot.2015.053; pmid: 25950237
43. T. B. Hiyama, T. Ito, H. Imataka, S. Yokoyama, Crystal structure of the α subunit of human translation initiation factor 2B. *J. Mol. Biol.* **392**, 937–951 (2009). doi: 10.1016/j.jmb.2009.07.054; pmid: 19631657
44. N. W. Moriarty, R. W. Grosse-Kunstleve, P. D. Adams, Electronic Ligand Builder and Optimization Workbench (eLBOW): A tool for ligand coordinate and restraint generation. *Acta Crystallogr. D* **65**, 1074–1080 (2009). doi: 10.1107/S0907444909029436; pmid: 19770504
45. P. Emsley, B. Lohkamp, W. G. Scott, K. Cowtan, Features and development of Coot. *Acta Crystallogr. D* **66**, 486–501 (2010). doi: 10.1107/S0907444910007493; pmid: 20383002
46. P. D. Adams *et al*., PHENIX: A comprehensive Python-based system for macromolecular structure solution. *Acta Crystallogr. D* **66**, 213–221 (2010). doi: 10.1107/S0907444909052925; pmid: 20124702
47. V. B. Chen *et al*., MolProbity: All-atom structure validation for macromolecular crystallography. *Acta Crystallogr. D* **66**, 12–21 (2010). doi: 10.1107/S0907444909042073; pmid: 20057044
48. S. J. Ludtke, Single-particle refinement and variability analysis in EMAN2.1. *Methods Enzymol.* **579**, 159–189 (2016). doi: 10.1016/bs.mie.2016.05.001; pmid: 27572727
49. P. Schuck, Size-distribution analysis of macromolecules by sedimentation velocity ultracentrifugation and lamm equation modeling. *Biophys. J.* **78**, 1606–1619 (2000). doi: 10.1016/S0006-3495(00)76713-0; pmid: 10692345

ACKNOWLEDGMENTS

We dedicate this work to the memory of Günter Blobel (1936–2018) and his foundational contributions to cell biology. We thank J. Peschek, E. Karagöz, R. Stroud, J. Fraser, G. Narlikar, R. Vale, A. Brilot, N. Schirle Oakdale, N. Talledge, P. Tsai, Ni Mu, J. Choe, C. Upjohn, M. Jacobson, C. Kalyanaraman, and the Walter and Frost labs for reagents, technical advice, and helpful discussions; M. Braunfeld, D. Bulkley, and A. Myasnikov of the UCSF Center for Advanced CryoEM and D. Toso and P. Tobias of the Berkeley Bay Area CryoEM Facility, which are supported by NIH grants S10OD020054 and 1S10OD021741 and the Howard Hughes Medical Institute (HHMI); Z. Yu, R. Huang, and C. Hong of the CryoEM Facility at the HHMI Janelia Research Campus; the QB3 shared cluster and NIH grant 1S10OD021596-01 for computational support; and G. Pavitt for the GP6452 yeast strain used in the purification of eIF2. The Titan X Pascal used for this research was donated by the NVIDIA Corporation.

Funding: Supported by a HHMI Faculty Scholar grant, the Searle Scholars Program, and NIH grant 1DP2GM110772-01 (A.F.) and by Calico Life Sciences LLC, the Rogers Family Foundation, the Weill Foundation, and HHMI (P.W.). A.F. is a Chan Zuckerberg Biohub Investigator, and P.W. is an Investigator of HHMI. **Author contributions:** Conception and design, analysis and interpretation of data: J.C.T., L.M.V., A.A.A., A.R.R., A.F., and P.W.; acquisition of data: J.C.T., L.M.V., A.A.A., P.J., and H.C.N.; writing (original draft): J.C.T., L.M.V., A.A.A., A.F., and P.W.; Writing (review and editing): J.C.T., L.M.V., A.A.A., P.J., H.C.N., A.R.R., A.F., and P.W. **Competing interests:** P.W. and A.R.R. are inventors on U.S. Patent 9708247 held by the Regents of the University of California that describes ISRIB and its analogs. Rights to the invention have been licensed by UCSF to Calico. **Accession numbers:** Accession numbers for the human eIF2B structures determined with FREALIGN, cryoSPARC, and RELION, respectively, are as follows: EMD-7442, EMD-7443, EMD-7444 (density maps; Electron Microscopy Data Bank) and 6CAJ (coordinates of atomic models; Protein Data Bank). **Data availability:** All data needed to evaluate the conclusions in the paper are present in the paper and/or the supplementary materials, and the structural data is available in public databases. All of the raw cryo-EM particle images are available upon request. The GP6452 yeast strain is available under a material transfer agreement with the University of Manchester.

SUPPLEMENTARY MATERIALS

www.sciencemag.org/content/359/6383/aaq0939/suppl/DC1
Supplementary Methods
Figs. S1 to S9
Tables S1 to S3

14 November 2017; accepted 9 February 2018
10.1126/science.aaq0939

Structure of the nucleotide exchange factor eIF2B reveals mechanism of memory-enhancing molecule

Jordan C. Tsai, Lakshmi E. Miller-Vedam, Aditya A. Anand, Priyadarshini Jaishankar, Henry C. Nguyen, Adam R. Renslo, Adam Frost and Peter Walter

Science **359** (6383), eaaq0939.
DOI: 10.1126/science.aaq0939

ISRIB mechanism of action

In rodents, a druglike small molecule named ISRIB enhances cognition and reverses cognitive deficits after traumatic brain injury. ISRIB activates a protein complex called eIF2B that is required for the synthesis of new proteins. Tsai *et al.* report the visualization of eIF2B bound to ISRIB at near-atomic resolution by cryo–electron microscopy. Biochemical studies revealed that ISRIB is a "molecular staple" that promotes assembly of the fully active form of eIF2B. Zyryanova *et al.* report similar structures together with information on the binding of ISRIB analogs and their effects on protein translation.

Science, this issue p. eaaq0939, p. 1533